

# Hemodynamics of the Hepatic Venous Three-Vessel Confluences Using Particle Image Velocimetry

MIKHAIL LARA,<sup>1</sup> CHIA-YUAN CHEN,<sup>1</sup> PHILIP MANNOR,<sup>1</sup> ONUR DUR,<sup>1</sup> PRAHLAD G. MENON,<sup>1</sup>  
AJIT P. YOGANATHAN,<sup>2</sup> and KEREM PEKKAN<sup>1</sup>

<sup>1</sup>Biomedical Engineering Department, Carnegie Mellon University, 5000 Doherty Hall, Pittsburgh, PA 15217, USA; and  
<sup>2</sup>School of Biomedical Engineering, Georgia Institute of Technology, Atlanta, GA, USA

(Received 31 December 2010; accepted 10 May 2011)

Associate Editor Laura Suggs oversaw the review of this article.

**Abstract**—Despite rapid advancements in the patient-specific hemodynamic analysis of systemic *arterial* anatomies, limited attention has been given to the characterization of major *venous* flow components, such as the hepatic venous confluence. A detailed investigation of hepatic flow structures is essential to better understand the origin of characteristic abnormal venous flow patterns observed in patients with cardiovascular venous disease. The present study incorporates transparent rapid-prototype replicas of two pediatric hepatic venous confluence anatomies and two-component particle image velocimetry to investigate the primary flow structures influencing the inferior vena cava outflow. Novel jet flow regimes are reported at physiologically relevant mean venous conditions. The sensitivity of fluid unsteadiness and hydraulic resistance to multiple-inlet flow regimes is documented. Pressure drop measurements, jet flow characterization, and blood damage assessments are also performed. Results indicate that the orientation of the inlets significantly influences the major unsteady flow structures and power loss characteristics of this complex venous flow junction. Compared to out-of-plane arranged inlet vessel configuration, the internal flow field observed in planar inlet configurations was less sensitive to the venous inlet flow split. Under pathological flow conditions, the effective pressure drop increased as much as 77% compared to the healthy flow state. Experimental flow field results presented here can serve as a benchmark case for the surgical optimization of complex anatomical confluences including visceral hemodynamics as well as for the experimental validation of high-resolution computational fluid dynamics solvers applied to anatomical confluences with multiple inlets and outlets.

**Keywords**—Particle image velocimetry, Patient-specific surgical planning, Hepatic blood flow, Hemodynamics, Flow instability, Jet flow.

## INTRODUCTION

The majority of patient-specific hemodynamic studies have focused on cardiovascular components of the arterial system, such as the carotid bifurcation (1-inlet and 2-outlet vessel configuration),<sup>3,38</sup> aortic arch (1-inlet, 4-outlet),<sup>34,57</sup> pulmonary arteries,<sup>31,71</sup> thoracic aorta,<sup>75</sup> and cerebral arterial vessels<sup>61</sup> providing valuable clinically relevant information. The venous flow components, in contrast, received relatively less attention except in studies that analyzed the fluid dynamics of arterio-venous grafts (2-inlet, 2-outlet),<sup>44</sup> cardiovascular devices,<sup>43</sup> and the total cavopulmonary surgical connection (2-inlet, 2-outlet).<sup>58</sup> Compared to the “upstream” arterial components, the “downstream” venous vessels are collective components, and thereby have a greater potential for flow unsteadiness<sup>56</sup> and coherent flow structures.<sup>77</sup> High vessel compliance of the venous system can generate physiological spontaneous intermittent flow, namely the “water-fall phenomena” as observed in extrathoracic-to-intrathoracic veins and in pulmonary veins. Furthermore, the adverse pressure gradient and increasing vessel area along the main flow direction make some venous vessels more vulnerable to internal flow instabilities, especially in the disease state and when cardiovascular devices are involved.<sup>64</sup> In the present study, the inherent flow unsteadiness of a major venous flow component, with 3-inlet and 1-outlet vessels, the hepatic/portal vein confluence, was analyzed using experimental fluid dynamics techniques. Particularly, outflow dynamics of the left hepatic vein (LHV), middle hepatic vein (MHV), and right hepatic vein (RHV) into the inferior vena cava (IVC) was investigated.

As in the arterial vessels, the venous vessel intima is covered by the “venous” endothelial cells, albeit in

---

Address correspondence to Kerem Pekkan, Biomedical Engineering Department, Carnegie Mellon University, 5000 Doherty Hall, Pittsburgh, PA 15217, USA. Electronic mail: kpekk@andrew.cmu.edu

lesser density, and governs mechanotransduction. In the arterial system, wall shear stress (WSS) loading depends strongly on the 3D flow structures.<sup>26</sup> Essentially similar phenomena are also observed in the venous wall.<sup>9</sup> Particularly in major hepatic diseases such as, portal hypertension and cirrhosis, vascular morphological changes are associated with WSS loading as indicated by the hemodynamic studies that are recently conducted.<sup>74</sup> In addition to vein bypass graft failure, and transplant vasculopathy, as well as venous valve diseases, in the venous system, “disturbed flow resulting from reflux, outflow obstruction, and/or stasis leads to venous inflammation and thrombosis,<sup>41</sup> and hence the development of chronic venous diseases”.<sup>9</sup> Chronic abnormal hemodynamic conditions at the hepatic junction will also influence the right-heart preload and blood-volume loading/balance that can lead to right-heart failure.

Achieving optimal hemodynamics through the hepatic/portal vein junction is also critical for the treatment of pediatric congenital heart diseases and their surgical palliation.<sup>16,17,25,59</sup> Hepatic flow influences the pulmonary/venous function, liver growth factor mixing,<sup>12,76</sup> abdominal venous flow augmentation<sup>29,70</sup> and plays a major role in adult “failed” Fontan physiology.<sup>15,35</sup> These conditions impact a significant number of young patients with heart defects (2 per 1000 live births). Poor visceral fluid dynamics and unbalanced hepatic lung growth factor distribution in surgical pathways especially are associated with pulmonary venous malformations.<sup>14,62,67</sup> Setyapranata,<sup>60</sup> reports that in a study of pediatric patients who underwent the Kawashima procedure, the majority of the patients developed pulmonary arteriovenous malformations (PAVMs). The abnormalities regressed after the completion of the Fontan procedure, which drained the hepatic effluent into the pulmonary circulation. Barbe,<sup>4</sup> provides further evidence of the hepatic regulation of PAVMs, reporting their occurrence in patients with liver failure. The malformations reportedly regress upon liver transplantation.

Blood flow from the hepatic venous system comprises a significant portion of the total visceral blood return (38%). Previous research utilizing both surgical and non-invasive interventions has highlighted a wide range of vascular complications associated with abnormal hepatic blood vessel anatomy. These abnormalities strain the visceral vascular network resulting in decreased outflow into the inferior vena cava (IVC) and increased blood retention in the liver. Carnevale *et al.*<sup>7</sup> reports that for pediatric patients having undergone liver transplantation, long-term success of the procedure may be negatively influenced by factors such as differences in the diameters of the

hepatic vein (HV) and IVC. The structural variations between the graft and host correlate with the presence of venous outflow obstruction and hydraulic resistance. High hydraulic power loss and effective pressure drop of the HV will decrease the hepatic effluent that drains into the inferior vena cava resulting in blood stasis, inadequate nutrient transport, and upstream vascular complications. Studies focusing on post-operative blood flow in pediatric liver transplantation have reported that despite successful graft transplant, it is common for the HVs to display flow patterns indicative of pathological conditions. Someda *et al.*<sup>65</sup> found that transplant recipients exhibiting uniform hepatic waveforms suffered from hepatic venous outflow obstruction and required balloon angioplasty. Both the phase and amplitude of the HV waveform have become an important diagnostic criterion for hepatic diseases such as the hepatic parenchymal disease.<sup>32,33</sup> Likewise, during liver transplant, or explant operations surgeons have the opportunity to ensure adequate reconstruction of the hepatic vessels to avoid poor hepatic outflow, as well as optimize for hemodynamic energy losses.

Hepatic venous circulation is also critical for understanding fetal hemodynamics.<sup>55</sup> During birth major hepatic shunts are spontaneously closed (e.g., ductus venosus). These rapid vascular morphological changes are likely to be influenced through flow-induced loading and the paracrine factors. Understanding the mature wall shear stress loading levels at the hepatic venous system will guide future studies that focus on fetal and neonatal hepatic circulation. Hepatic vascular development has a major impact on the proper function of the liver.

*In vivo* characterization of visceral circulation through different image modalities has only recently become possible due to the intense diaphragm motion artifacts of the hepatic vessels. For example, Cheng<sup>8</sup> and Mehran<sup>46</sup> used Doppler ultrasonography and cadaveric studies, respectively, to acquire the physiological anatomy. Similar studies were performed in animal models to quantify wall shear stress loading.<sup>74</sup> Using patient-specific three-dimensional (3D) cardiac magnetic resonance image (MRI) reconstructions, Yang<sup>79</sup> and George<sup>24</sup> performed pioneering computational fluid dynamics analyses of the portal vein blood flow. Their results revealed that for patients afflicted with cirrhosis, the flow field inside the portal vein exhibits significantly decreased velocity per liver volume and lower hemodynamic unsteadiness. In comparison, the present study focuses on the downstream liver circulation and entirely employs experimental techniques. The main objective is to perform a detailed investigation on physiological hepatic flows through bench-top particle image velocimetry experiments as a

first step towards a comprehensive understanding on the origin of characteristic abnormal venous flows patterns.

The manuscript is organized as follows: first, the protocols for generating the anatomical computer-aided design models and transparent rapid-prototype replicas of two pediatric hepatic vein confluences with 3-inlets and 1-outlet vessels are described, followed by *in vitro* flow visualization, pressure measurements, and PIV experimental methodology. Hemodynamic parameters to quantify the effective pressure drop, characterize the jet flow, and predict the relative blood damage at both healthy and pathological conditions are defined. Detailed flow analysis including flow field characterization, viscous shear, Reynolds stress, and hydraulic performance evaluation are presented in the “[Results](#)” section. Hemodynamic interpretation of novel findings, potential outcomes and limitations are described in the “[Discussion](#)” and “[Conclusions](#)” sections. To our best knowledge, this study presents the first comprehensive fluid dynamic characterization of the hepatic venous confluence *in vitro*.

## METHODS

### *Transparent Patient-Specific Anatomical Model Fabrication*

Patient-specific 3D anatomies of the confluence region, which is comprised of the three major infra-diaphragmatic hepatic veins, were reconstructed from cardiac MRI scans of two pediatric patients having normal hepatic venous anatomies. MRI is the preferred and accurate method for acquisition of complex 3D anatomical vessels data.<sup>50</sup> Hepatic Vein Model-1 (HV1) and Hepatic Vein Model-2 (HV2), shown in Fig. 1, were selected to feature two structural differences that are suspected to contribute to the complex fluid flow characteristics in the confluence. Primarily, the planar alignment of the inlet vessels is significantly different between these two models. In the HV1 model, all three hepatic veins are oriented on the horizontal plane whereby featuring an in-plane cross-flow mixing within the common pouch region. In contrast, model HV2 has two inlet vessels, the left hepatic vein (LHV)

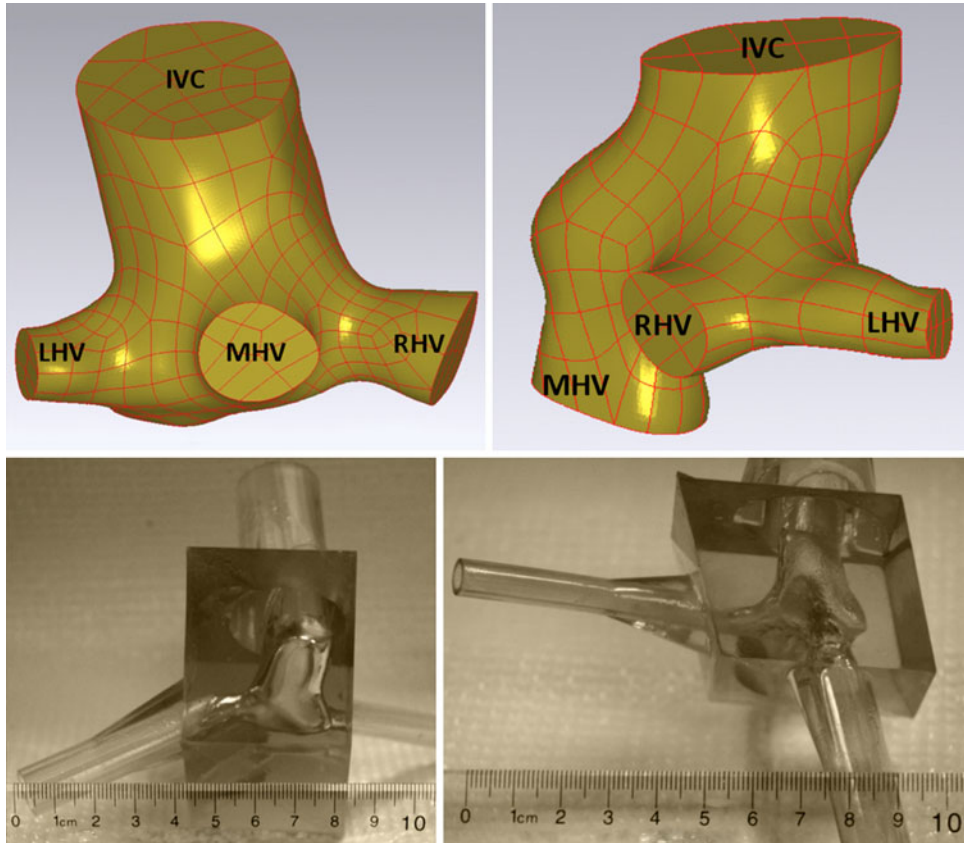


**FIGURE 1.** The two subject-specific hepatic vein (HV) junctions, HV1 (left) and HV2 (right), studied using particle image velocimetry and pressure drop experiments. Computer-aided design files (top row) and corresponding transparent stereolithographic prototypes (bottom row) of the vein geometries display the orientations of the inlets relative to the IVC outflow. IVC, inferior vena cava; LHV, left hepatic vein inlet; RHV, right hepatic vein inlet; MHV, middle hepatic vein.

and right hepatic vein (RHV), oriented approximately 90° out-of-plane from the third inlet, i.e., the middle hepatic vein (MHV). Secondary to this main geometrical feature, MHV is positioned at an offset location such that only the LHV and RHV generate cross-flow mixing within HV2 as opposed to the in-plane mixing of all hepatic inlets in HV1. These differences represent a subset of anatomical variations that are typically observed in both healthy and surgically reconstructed venous vessel junctions. The corresponding NIH Anatomical Database identifications of HV1 and HV2 are CHOA012 and CHOA004, respectively.

The point-cloud patient data was segmented to isolate the junctions of the three major hepatic veins to the IVC (Geomagic Studio 10, Durham, NC). After minimal smoothing, the digital model was converted into NURBS patches in IGS format. The NURBS data was imported into Pro/Engineer software (Needham, MA) to create a negative of the vein geometry. To attach tubing and avoid entrance length affects, the inlets were extended from the vein junction maintaining the anatomical vessel shape. The wall thickness was minimized to reduce laser power intensity losses. The volumetric shell was split into two halves and converted into STL file format to be compatible with commercial rapid-prototyping systems.

Both hepatic venous junction models were fabricated by direct stereolithographic printing (Fineline Inc, Raleigh, NC), using a high clarity liquid photopolymer resin (DSM Somos Watershed XC11122).<sup>10,30,68</sup> Before assembly, the surfaces (bonded by a clear epoxy resin)

were sanded using decreasing grid sizes of 400 grit, 600 grit, and 1  $\mu\text{m}$  grit papers. All model surfaces were treated with polishing compounds (No. 2 “Fine Scratch Remover” and No. 1 “Plastic Clean & Shine”). Surfaces corresponding to the internal vein geometry were not sanded. The method used to fabricate the vein geometry from clinical data follows the process described in detail by de Zelicourt *et al.*<sup>13</sup> and Pekkan *et al.*<sup>54</sup>

### *In Vitro Flow Loop*

A steady bench-top flow loop was constructed using PVC pipes and tygon tubing, Fig. 2. Vein inlet alignment rods with a minimum length of 12 inches eliminate spurious flow structures and facilitate the transition to fully developed flow at the vessel inlets. Pressure head to drive flow through the loop was supplied by means of a variable-speed submersible steady flow pump, which drained into an elevated head tank. Both vein models were mounted on an adjustable platform to control the laser sheet orientation relative to the laboratory frame of reference. The laser sheet was oriented at an angle of 41° from vertical so that a 5 mm decrease in the platform height resulted in a 3.75 mm translation of the measurement plane. A rotameter was positioned at the IVC outflow for recording the total flow rate. Flow rates through individual vessel segments were adjusted using valves placed at the LHV and MHV inlets. Flow through the RHV segment was controlled using a variable setting tubing clamp and determined based on the conserva-

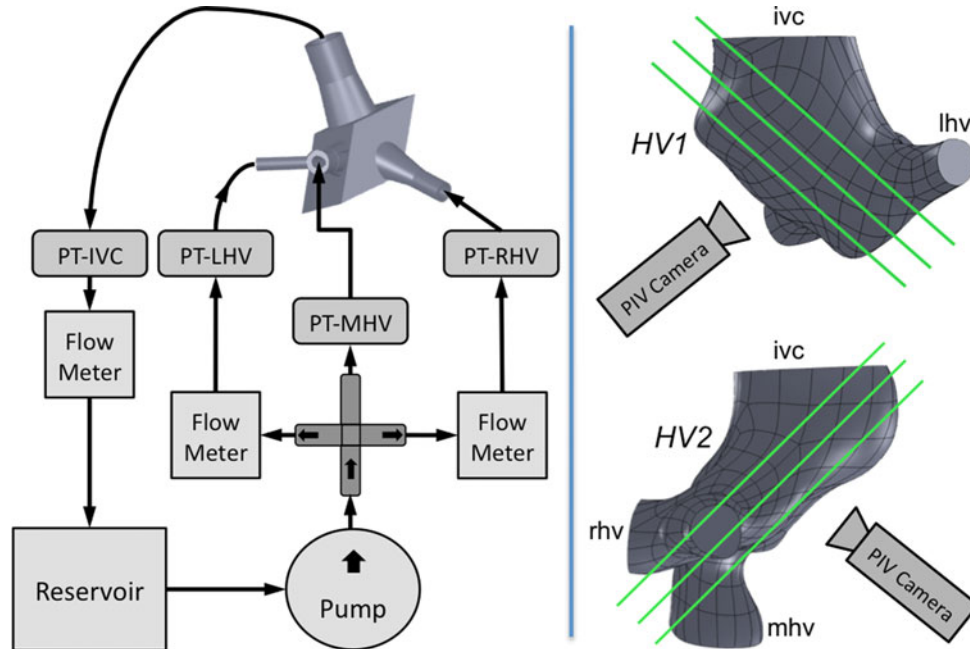


**FIGURE 2.** Schematics of the flow loop (left) and laser sheet orientations for both models HV1 and HV2 (right) with respect to the camera. PT denotes a pressure transducer.



tion of mass principle using the flow measurements at the inlets and outlet. This system allowed us to accurately set the flow splits to simulate physiological (LHV/MHV/RHV: 0.4/0.4/0.2) and pathological flow rates (LHV/MHV/RHV: 0.3/0.4/0.2) reported in literature.<sup>27–29,48,69,72</sup> The experimental flow conditions are tabulated in Table 1. These flow conditions are labeled “healthy” and “pathological” according to the clinical diagnoses of pediatric patients. “Pathological” flow conditions correspond to the mean hepatic flows reported for children diagnosed with acute hepatic disease.<sup>48</sup>

Pressure measurements were performed through the pressure taps located less than 1 cm from the inlets and outlet of the each model. Pressure transducers (Edwards Life Sciences, Irvine, CA) and amplifier instrumentation (WPI Inc., Sarasota, FL) were calibrated through standard procedures before and after each experiment to eliminate any hysteresis error.

The working fluid used in all the experiments was a freshly prepared solution of saturated sodium iodide, glycerin, and deionized water at a volumetric ratio of 75:24:1, respectively. The kinematic viscosity of the blood analogue was  $3.5 \pm 0.1$  cSt, measured with a bulb viscometer, and the refractive index was measured to be 1.50, matching the index of the resin model. This mixture ratio is identical to fluids used in PIV studies of venous flows<sup>16,17,59</sup> and physiological values for blood at high shear rates.<sup>42,49</sup> Fluorescent polymer microspheres with a mean diameter of  $8 \mu\text{m}$  (Duke Scientific Corp.) and excitation and emission wavelengths of 542 and 612 nm, respectively, were added to

the analogue for flow visualization. The addition of fluorescent particles did not measurably affect the viscosity or refractive index of the blood analogue.

### PIV System and Data Processing

A standard PIV system was used to acquire two-component velocity field measurements for each model at three planes spaced 3.75 mm apart having a laser sheet thickness less than 1.5 mm, Fig. 2. The system consisted of two Nd:YAG lasers (Model Twins BSL 50, Quantel) with an energy of 50 mJ per pulse at 532 nm and operated at a repetition rate of 15 Hz. The laser was positioned so the laser sheet aligned parallel to the camera lens to minimize distortion. The image pairs were recorded using a CCD camera (Model Imager Pro X 2M, LaVision, Germany) with a  $1600 \times 1200$  pixel resolution. The camera was fitted with a high pass filter to block laser light (532 nm) and to transmit fluorescent microsphere light to the CCD.

A series of image pairs were acquired at spatial resolution of  $40 \mu\text{m}/\text{pixel}$  for each PIV plane. Laser pulse delay times of 2000 and 2500  $\mu\text{s}$  were used to maximize particle image displacement without loss of correlation for an initial interrogation window size of  $32 \times 32$  pixels and a final interrogation window size of  $16 \times 16$  pixels. Interrogation windows were overlapped by 50% to satisfy the Nyquist sampling criterion. The effect of pulse separation time on velocity field results is also tested. All processed data acquired with 2000 and 2500 ms pulse separation delays resulted in a maximum of 10% difference (locally) of the measured velocity magnitudes. Convergence was achieved in the running average velocity value (both maximum and average) after  $\sim 100$  image pairs, still 300 image pairs were used in all calculations. The dynamic velocity range,<sup>66</sup> ratio of the maximum velocity to the minimum resolvable velocity, of this PIV set-up was estimated to be 179 using the theory developed by Adrian.<sup>2</sup> The root-mean-square velocity measurement error is 1.4 mm/s, and the minimum resolvable velocity fluctuation was acceptably small in comparison with the maximum flow speed of 0.25 m/s. Vector field post-processing was performed using Matlab (Mathworks, Natick, MA).

### Hemodynamic Parameters

#### Jet Profiles and Vorticity

The spatial development of the jet flows was analyzed using velocity profiles and vorticity distribution. The profiles for each model were acquired at five locations describing the characteristic jet evolution for healthy and pathological flows. The 2D vorticity was

**TABLE 1. Flow rates and Reynolds numbers (given in parenthesis) specified during the particle image velocimetry acquisition (H and P) and pressure drop measurements (1–4) for hepatic vein models HV1 and HV2.**

Flow setting	Flow units (L/min) ( <i>Re</i> )			
	$Q_{\text{IVC}}$	$Q_{\text{LHV}}$	$Q_{\text{MHV}}$	$Q_{\text{RHV}}$
<b>HV1</b>				
Healthy (H)	1 (433)	0.4 (303)	0.4 (242)	0.2 (202)
Pathological (P)	1 (433)	0.3 (227)	0.4 (242)	0.3 (303)
1	0.76	0.30	0.30	0.15
2	0.95	0.38	0.38	0.19
3	1.14	0.45	0.45	0.23
4	1.51	0.61	0.61	0.30
<b>HV2</b>				
Healthy (H)	1 (303)	0.4 (151)	0.4 (269)	0.2 (202)
Pathological (P)	1 (303)	0.3 (113)	0.4 (269)	0.3 (303)
1	0.76	0.30	0.30	0.15
2	0.95	0.38	0.38	0.19
3	1.14	0.45	0.45	0.23
4	1.51	0.61	0.61	0.30

Average vessel hydraulic diameters of IVC, LHV, MHV, and RHV are: 7, 4, 5, 3 and 10, 8, 4.5, 3 for HV1 and HV2, respectively, in mm.

calculated using a second-order central difference template:

$$\omega = \left( \frac{\partial v}{\partial x} - \frac{\partial u}{\partial y} \right) \quad (1)$$

### Shear Stress and Parameters for Unsteadiness

The viscous stress tensor  $\tau_{ij}$  was calculated using the standard incompressible Newtonian fluids formulation, Eq. (2), where  $\mu$  is the dynamic viscosity,  $u_i$  is velocity component, and  $x_i$  is the corresponding a spatial coordinate. Derivative terms were estimated by second-order central differencing of the average velocity field.

$$\tau_{ij} = \mu \left( \frac{\partial u_i}{\partial x_j} + \frac{\partial u_j}{\partial x_i} \right) \quad (2)$$

To establish a coordinate-independent measure of the shear stress tensor, the principal viscous shear stress (PVSS) throughout the flow field was computed from Eq. (3), where  $\sigma$  indicates the eigenvalue of the stress tensor.

$$\tau_{PVSS} = \frac{1}{2}(\sigma_{\max} - \sigma_{\min}) \quad (3)$$

Based on the Reynolds averaged Navier–Stokes equations for turbulence modeling, Reynolds stresses ( $R_{ij}$ ) indicate the average momentum transfer between the fluctuation velocity and the mean velocity, and provide proper analysis indices for flow unsteadiness. In unsteady fluid flow regimes,<sup>18,19,23,52</sup> Eq. (4) provides a measure for the amount of fluctuation in the velocity field ( $\rho$  is the fluid density and  $\mu'_i$  indicates the fluctuation in the velocity component).

$$R_{ij} = \rho \overline{u'_i u'_j} \quad (4)$$

Since these nine Reynolds stress components comprise a second-order tensor, the principal Reynolds shear stress (PreSS) is calculated similar to the PVSS, Eq. (3).

The non-dimensional correlation coefficient governs strength of correlation among flow fluctuation terms<sup>73</sup> and given by Eqs. (5) and (6), with respect to a fixed 2D Cartesian ( $x$ – $y$ ) and locally variable streamwise-normal curvilinear coordinate system, respectively.

$$C_{xy} = \frac{\overline{u_x u_y}}{\left( \overline{u_x^2} \cdot \overline{u_y^2} \right)^{\frac{1}{2}}} \quad (5)$$

$$C_{sn} = \frac{\overline{u_s u_n}}{\left( \overline{u_s^2} \cdot \overline{u_n^2} \right)^{\frac{1}{2}}} \quad (6)$$

The standard correlation coefficient is an unbiased description of the mean unsteadiness compared to the

Reynolds stresses as it is normalized by the square root of the product of the mean variances of the velocity fluctuations. The correlation coefficient range from  $-1$  to  $1$  can be interpreted as being the mean correlation of fluctuations in orthogonal velocity components.<sup>73</sup> Bradshaw *et al.*<sup>6</sup> used this parameter for studying free-jet turbulence to quantify the degree of Reynolds shear stress in the mixing region, the boundary layer, and the asymptotic jet region. Since flow directionality is important in the present study the velocity fluctuations in the direction of the average flow streamlines are also calculated. Regions of large correlation coefficient values for this *moving coordinate system* are indicative that the mean axes of velocity fluctuation are closely aligned with the average fluid paths.

### Pressure Drop, Energy Loss, and Blood Damage

For multi-inlet, multi-outlet components the *effective* pressure drop ( $\Delta P_{\text{eff}}$ ) of the conduit is defined based on the control volume power loss ( $P_{\text{loss}}$ ) and formulated as follows:

$$P_{\text{loss}} = \sum_{\text{INLETS}} (PQ) - \sum_{\text{OUTLETS}} (PQ) \quad (7)$$

$$\Delta P_{\text{eff}} = \frac{P_{\text{loss}}}{Q_{\text{total}}} \quad (8)$$

The pressure drop depends on flow conditions, including flow rate  $Q$  and geometry. Studies report that changes as high as 12% can result from minor differences in inlet flow conditions.<sup>56</sup> For HV geometries, the effective pressure drop was reported at physiological and pathological flow conditions to characterize their respective flow dependency measures.

Similar to the empirical red blood cell (RBC) damage model of Gierpielen *et al.* that is based on the laminar Couette flow experiments,<sup>37,53</sup> the flow shear stress and exposure time was used to estimate hemolysis due to the excessive viscous stresses and the unsteady velocity fields. Streamline averaged shear stresses and exposure times were calculated from the principal viscous shear stress and the time-averaged velocity field along the streamwise direction, respectively.

## RESULTS

### Major Flow Structures and the Velocity Field

Contour plots of velocity magnitude for model HV1 are presented in Fig. 3. The plots reveal the presence of two high-velocity jets that both generate large-scale recirculation regions. The dominant jet flow originates at the RHV inlet and extends across the main HV cavity reaching a maximum velocity of 25 cm/s. RHV

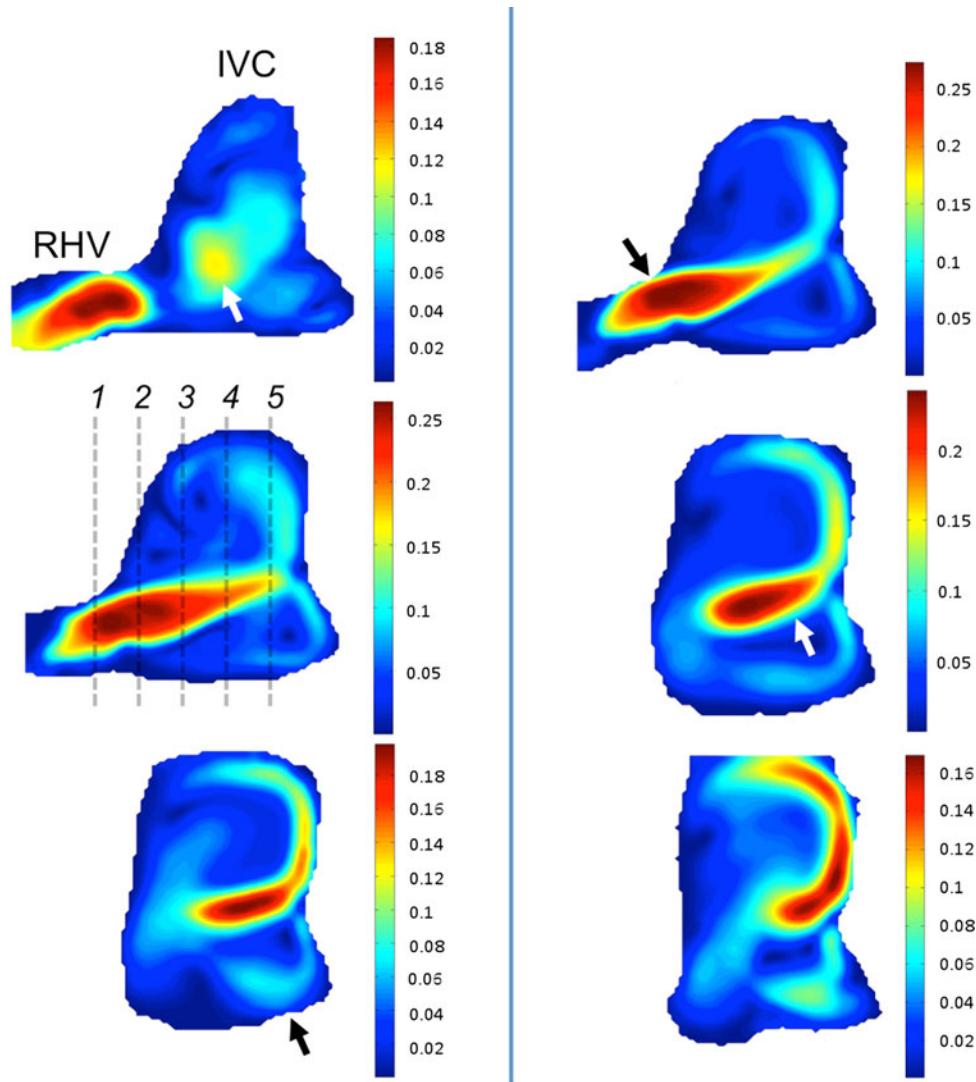


**FIGURE 3.** Two-component converged running average velocity magnitude distributions along the three PIV measurement planes (tracing mid RVH (top) towards the posterior direction (bottom)) of HV1 model for healthy (left) and pathological (right) flow conditions. Orientations of the acquisition planes are provided in Fig. 2. Color legend units are in m/s. IVC, inferior vena cava; RHV, right hepatic vein. Arrows highlight major flow structures. Numbers indicate the locations of jet profiles extracted for Fig. 5.

jet stagnates at the left wall and splits into upper and lower wall streams that form secondary recirculation regions at the anterior and posterior regions of the vein geometry. The second jet-like flow structure appears near the center of the vein pouch due to the out-of-plane MHV and LHV inlet flows. Similar to the RHV jet, the MHV jet has a principal direction towards the far wall and contributes to the formation of the jet structure located at the upper wall. The combined RHV and MHV jet structures play a major role in sustaining the recirculation region proximal to the IVC through the bifurcated wall jet structures.

Despite the in-plane cross-flow inlet orientation of HV1, the shift from healthy to pathological flow

settings affects only the velocity magnitudes within the venous confluence and does not alter the shape of the major fluid structures. For pathological flow settings, the dominant jet flow at the RHV inlet strengthens and extends across the main hepatic cavity terminating at the far wall and splits into an upper and lower wall jet. The MHV jet is also present, exhibiting a maximum velocity of 24 cm/s at the vein center and extending up the far wall along a curved path. The stagnating and bifurcating jet layer at the wall generates large recirculation regions in the hepatic junction.

Measured velocity magnitude distributions for HV2 at healthy and pathological flow conditions are presented in Fig. 4. A high velocity wall jet located

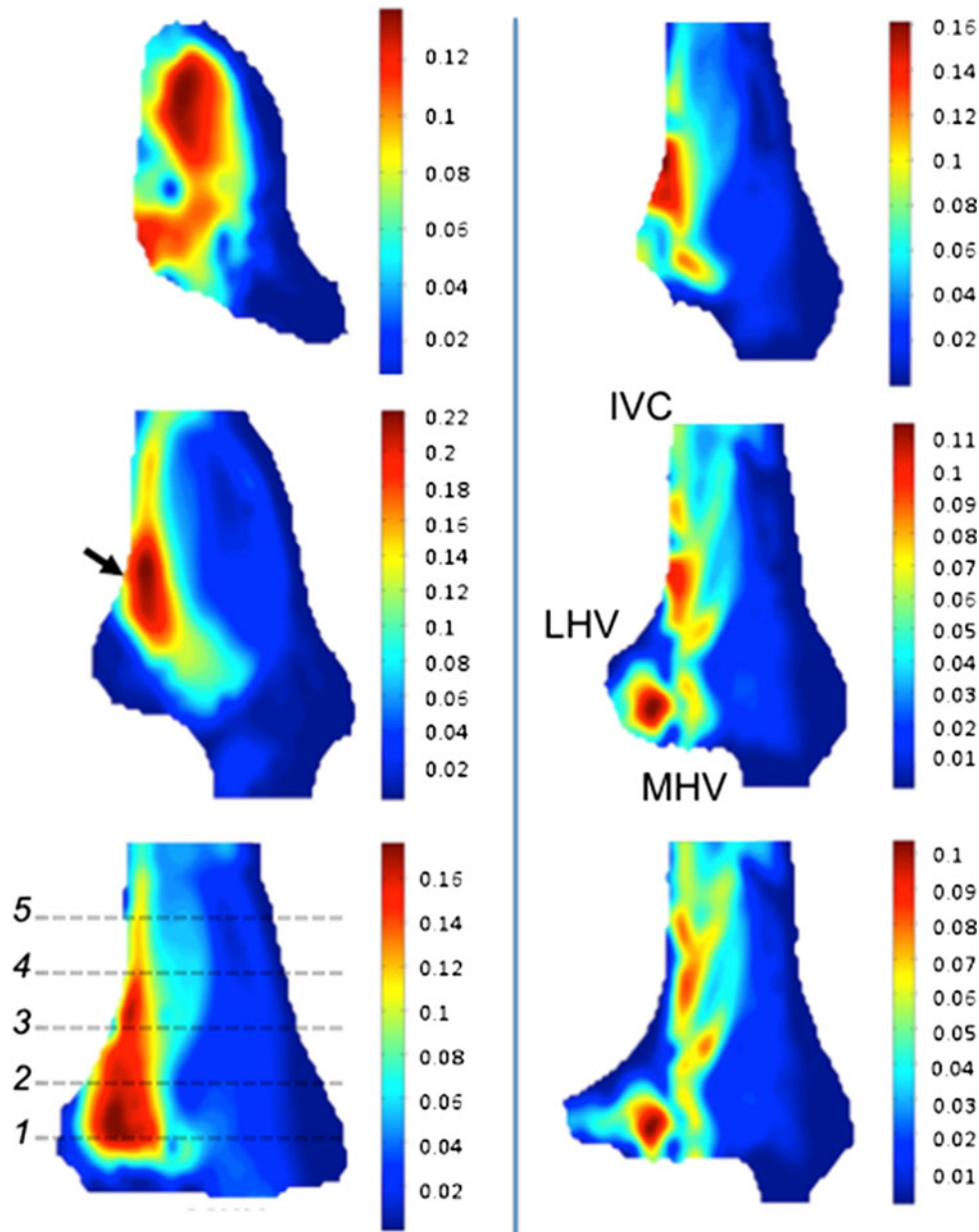


**FIGURE 4.** Two-component converged running average velocity magnitude distributions along the three PIV measurement planes (tracing mid RVH (top) towards the posterior direction (bottom)) of HV2 model for healthy (left) and pathological (right) flow conditions. Orientations of the acquisition planes are provided in Fig. 2. Color legend units are in m/s. IVC, inferior vena cava; LHV, left hepatic vein; MHV, middle hepatic vein. Arrows highlight major flow structures. Numbers indicate the locations of jet profiles extracted for Fig. 5.

immediately adjacent to the LHV inlet was identified as the dominant flow structure for the selected PIV plane orientation. The jet originates at the mixing region close to the bottom of the HV pouch located proximal to the confluence of the LHV and RHV flow streams. For healthy flow conditions, the core jet reaches a maximum velocity of 22 cm/s midway above the left wall and decays to 12 cm/s at the IVC outlet. The remaining portion of the HV geometry features a well-defined low velocity region with a peak velocity

close to 6 cm/s. Shift of the inlet flow splits for the pathological flow setting leads to noticeable changes in velocity magnitude distribution throughout the HV2. As seen for the healthy flow condition, the characteristic flow structure for the pathological flow state also manifests as a wall jet that originates at the LHV–RHV cross-flow region and remains localized near the left wall as it propagates towards the IVC. In contrast to the healthy flow condition, the pathological wall jet is significantly less structured, presenting intermittent



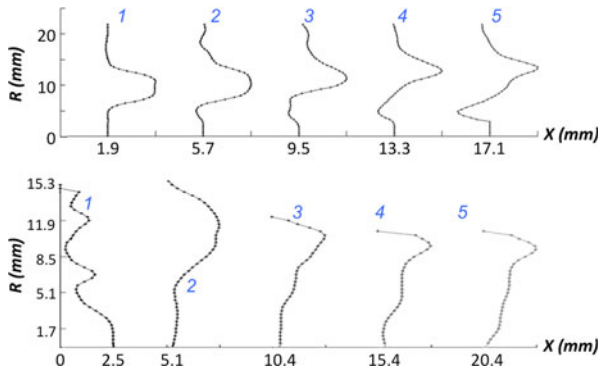


**FIGURE 5.** Development of the primary venous jets for models HV1 (top) and HV2 (bottom) at healthy flow split settings. Locations of velocity profiles are marked in Figs. 3 and 4. Velocity profiles are normalized with peak flow velocity.

regions of high velocity. The jet-core region has a maximum velocity of 16 cm/s midway from the left wall with a secondary lower velocity peak at 11 cm/s in the cross-flow mixing region. This high velocity region decays quickly, decreasing from 16 to 6 cm/s before reaching the IVC outlet.

#### Jet Flow Analysis

For the main jet flow structures at the healthy flow split settings, the time-averaged velocity profile development at selected axial locations are plotted in Fig. 5. Both anatomies demonstrated significant differences in their velocity profile development. For model HV1, the RHV jet enters the main junction cavity with a plug-shaped velocity profile. As the jet extends across the vein junction, the velocity profile becomes rounded until it attains a sharp parabolic profile at a distance of 9.5 mm from the RHV inlet. At 13.3 mm, the jet profile becomes stable with even sharper and central peak. Once the jet-core reaches to the far IVC, it is influenced from the vessel wall augmenting the backflow region. At pathological flow conditions jet profiles within the HV1 did not change significantly as pictured qualitatively in Fig. 3. For both healthy and pathological HV1 flow split conditions, the plug-to-parabolic profile development resembles the classical structural characteristic of a free-jet flow.<sup>1</sup> Vorticity contours of HV1 feature a pair of self-similar clockwise and counterclockwise rotating (negative and positive signed) regions surrounding the low vorticity RHV jet-core with maximum magnitudes of  $\pm 150 \text{ s}^{-1}$  (Fig. 6). The pathological 30% increase in RHV inlet flow led to an increase only in the negative vorticity magnitude (quantitative data not shown).

For HV2 anatomy, jet flow profiles indicate that the characteristic wall jet structure is strongly dependent

on inlet flow split due to the cross-flow oriented LHV and RHV vessels, Fig. 4. For healthy flow conditions, the wall jet evolves coherently and follows a progressive growth from a plug shape to a parabolic profile near the outlet to the IVC, as shown in Figs. 4 and 5. The flat profile region is predominantly associated with the cross-flow of the LHV and RHV streams. The velocity peak is located 10 mm anterior to the cross-flow region and continues to become more rounded as it approaches the IVC outlet 20 mm above the LHV–RHV cross-flow. The pathological flow split disrupted the wall jet characteristics and resulted in a distinct “twin-peak” profile that is present throughout the entire length of the jet. The magnitudes of the two peaks are found to be equal at the cross-flow region. The velocity peak closer to the wall decays to less than 50% of the maximum jet velocity 5 mm above the cross-flow while the right jet becomes the dominant jet peak. At 10.2 mm above the cross-flow, the jet profile remains relatively stable maintaining its structure as it reaches the IVC.

In simple jet flows, vorticity is primarily generated in the shear boundary layer surrounding the irrotational jet-core. The multi-inlet hepatic junctions feature additional complexity due to the orientation of the inlet jets relative to each other and wall influence. To verify the observed jet-like flow structures and to determine how the jets affect each other, specifically with regards to the jet orientation, the vorticity distribution of the average velocity field is calculated for the mixing flow (Fig. 6). Vorticity fields for healthy and pathological flows indicate a significant change in the sign and magnitude of fluid rotation associated with the HV2 wall-bounded jet. The vorticity of healthy flows is predominantly clockwise fluid rotation throughout the HV2 geometry with positive vorticity occurring at a small region along the left wall with a maximum of  $250 \text{ s}^{-1}$ . The pathological vorticity fields are plotted in Fig. 6. These indicate a significant decrease in overall vorticity magnitude from the healthy flow with the maximum vorticity decreasing to  $80 \text{ s}^{-1}$ . In addition, the pathological vorticity field features regions of positive and negative vorticities scattered throughout the wall jet region (Fig. 6), which were absent from the uniform jet structure of healthy flow condition. Examination of the vorticity distributions for the different flow conditions permits the measurement of the degree of sensitivity of the inlet jets to neighboring inlet flow conditions.

#### Viscous Shear Stress Distribution

For healthy flow regime of HV1 anatomy, a paired high stress region originating from the RHV inlet and

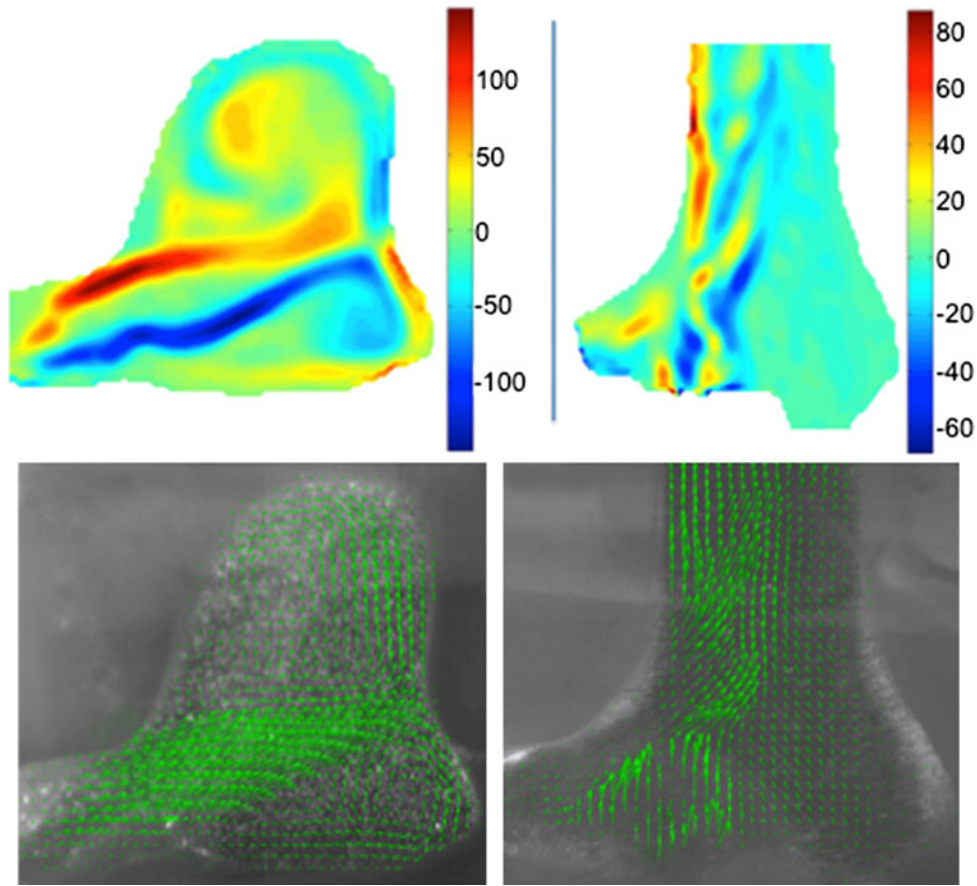


**FIGURE 6.** Vorticity (1/s) contour plots of HV1 for healthy (left) and HV2 for pathological flow splits (right). The flow field is structured with intermittent regions of clockwise (blue) and counter-clockwise (red) rotation. For HV1 jet flow stagnation is captured by the vorticity sign change close to the wall, generating additional shear layers in the junction. Vorticity is calculated from the average velocity vector field overlapped on the raw PIV data (lower row).

extending across the venous junction was the most noteworthy pattern (Fig. 7). This paired stress layers showed the highest principal stress values on the order of  $10 \text{ dyne/cm}^2$  and surround a core region of slightly lower shear stress. This structure extends up the vessel wall opposite to the RHV along a leftward turning lumen curvature. The low-stress core and pairing of positive and negative stress values are associated with the free-jet flow structure discussed earlier. The corresponding  $xy$ -stress plots are similar but not shown in the present article.

In general, the shear stress fields for pathological flow conditions in HV1 are similar to the healthy flows (Fig. 7). Inferior and superior shear stress layers that surround a central low-stress core region accompany the RHV jet. The maximum principal stress associated with the RHV jet occurs along the inferior shear layer at a value of  $20 \text{ dyne/cm}^2$  along the vessel wall. The centrally located jet structure demonstrates a similar shear layer pattern. It reaches maximum value of  $10 \text{ dyne/cm}^2$  proximal to the vessel wall.

The viscous shear stress distribution throughout the HV2 geometry indicates higher stress values for the healthy flow. As illustrated in Fig. 8, the wall-bounded jet extending towards IVC from the LHV–RHV cross-flow generates regions with high shear stress at the order of  $10 \text{ dyne/cm}^2$ . The highest stress region, with a PVSS of  $25 \text{ dyne/cm}^3$ , is located along the left wall in close proximity to the peak velocity. The contour plots of  $xy$ -shear stress distributions display the positive and negative pairings of the wall-bounded jet more clearly (Fig. 8).

Viscous stress distribution for the HV2 pathological flow exhibited less ordered structures and lower stress magnitudes relative to the healthy state. The majority of the principal stresses in all PIV planes were less than  $11 \text{ dyne/cm}^2$ . The peak stress regions were less localized along the left wall, in contrast to the healthy flow regime. Both the principal stress and  $xy$ -stress distributions feature large stress regions close to the LHV–RHV cross-flow as is propagates towards the IVC while remaining detached from the solid vessel

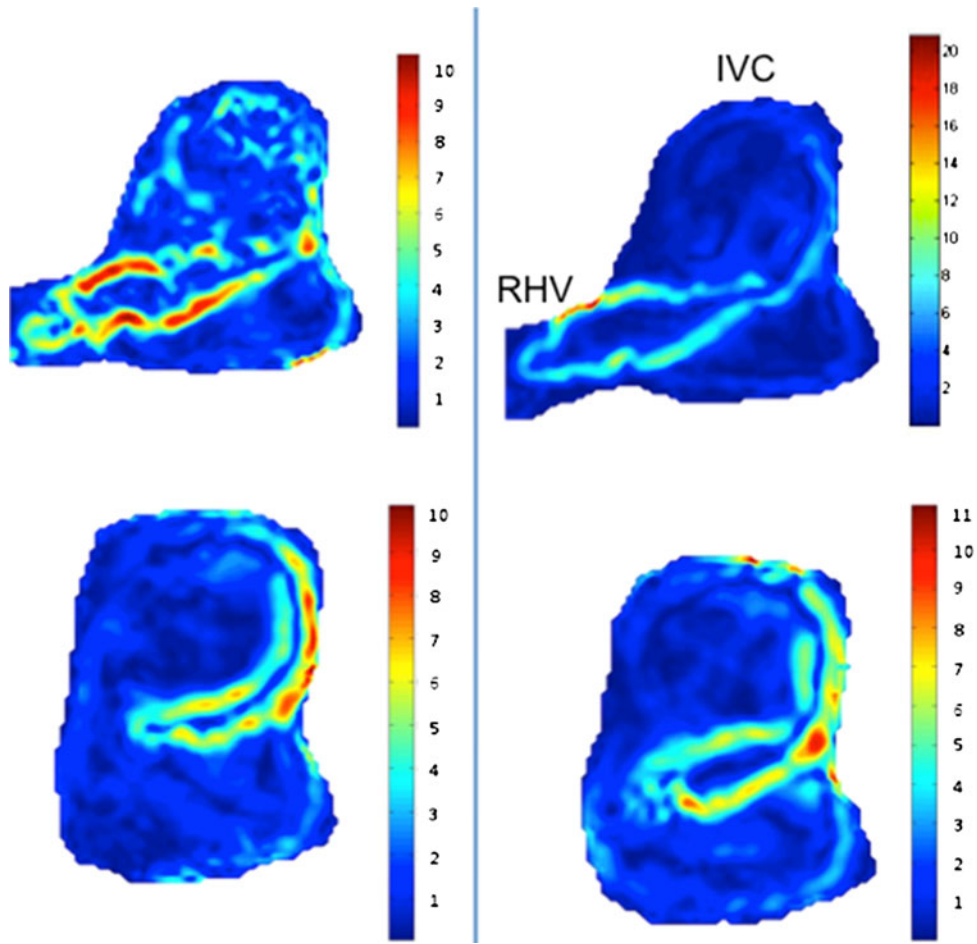


**FIGURE 7.** Principal shear stress distribution of the HV1 venous junction model for two consecutive PIV slices tracing the internal RHV jet structure. The structure of the shear layers of the RHV jet and MHV jet maintain the same organization for both flow settings (healthy (left) and pathological flow (right)). Shear stress units are in dyne/cm<sup>2</sup>.

wall. The  $xy$ -stress reveal interesting paired regions of positive and negative shear stress. These stress pairs originate at the LHV and as they approach the IVC outlet, reduce their magnitude significantly.

The complex shear stress loading observed in hepatic venous junctions suggested the possibility of increased blood damage within the three-vessel confluence. The time-averaged PIV data allowed the calculation of mean shear stress and exposure times during blood cell passage. These calculations showed that both vein geometries expose blood to moderate shear stresses but over short exposure durations. For both HV1 and HV2, mean shear stress is consistently calculated to be on the order of 10 dyne/cm<sup>2</sup> and exposure time on the order of  $10^{-3}$  s. The mean shear stress values uniformly decrease for both geometries when flow was changed from healthy to pathological flow settings, 10% for HV1 and 19% for HV2. The alteration of flow conditions did not result in any discernable differences in exposure time for either model. However, shear stresses uniformly decreased

for HV1 when flow was switched from healthy to pathological settings.

#### *Flow Unsteadiness and the Reynolds Stress Components*

The pouch-like venous confluence lumen and counter flowing jet-like structures generated recognizable flow unsteadiness and local flow instability. Reynolds stresses and principal Reynolds shear stress characterize the unsteadiness of the flow field due to the presence of the dominant jet flows. Figure 9 shows the distribution of the Reynolds shear stress for both models. For HV1, the RHV jet hosts the region of high velocity fluctuations at both healthy and pathological flow conditions. The presence of high values for principal Reynolds shear stress in the RHV inlet region, with a maximum of 80 dyne/cm<sup>2</sup>, provides strong evidence that unsteadiness is created in the venous junction due to fluctuations of the RHV jet flow. Pathological flow conditions are similar to healthy flow

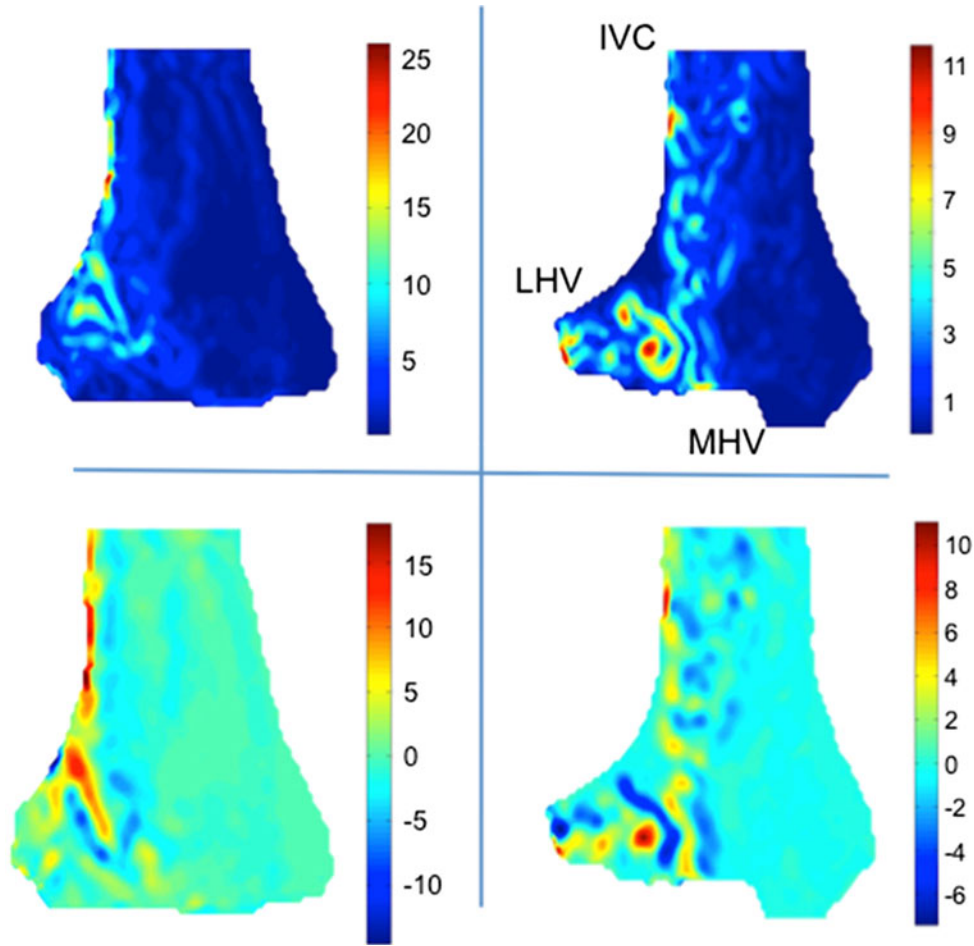


**FIGURE 8.** Contour plots of principal (top) and Cartesian,  $\tau_{xy}$  (bottom row) viscous shear stress in the HV2 vein junction. The viscous stresses remain localized at the left wall for healthy flow settings (left) and extend into the vein junction for pathological flows (right). Principle and Cartesian shear stress components demonstrate similar patterns. Units for both parameters are in dyne/cm<sup>2</sup>.

conditions because instabilities present in the RHV jet are the primary source of observed velocity fluctuations as the highest principal Reynolds shear stress reached to 50 dyne/cm<sup>2</sup>. It is important to note that despite the 33% increase in RHV flow, maximum PReSS value in the RHV jet decreased by 38% compared to the healthy flow.

For HV1, the normal Reynolds stress ( $R_{jj}$ ) reaches a maximum value of 160 dyne/cm<sup>2</sup> and maintains a magnitude of 100 dyne/cm<sup>2</sup> throughout that region. The principal Reynolds shear stress has a similar distribution as  $R_{jj}$ , with its maximum value reaching 90 dyne/cm<sup>2</sup> near the LHV–RHV cross-flow. For the pathological flow conditions, the  $R_{jj}$  and principal Reynolds shear stress contour plots in the cross-flow region exhibit similar spatial distributions. The maximum value for  $R_{jj}$  in the cross-flow region is 70 dyne/cm<sup>2</sup> with minor hot spots elsewhere in the venous junction. The maximum principal Reynolds shear stress value in the cross-flow region is 40 dyne/cm<sup>2</sup>.

The distributions of streamwise correlation coefficient of velocity fluctuations are shown in Fig. 10. For HV1 anatomy, high correlation values were observed along the primary jet direction. The velocity fluctuations observed are similar for healthy and pathological flows. At main recirculation regions, the streamwise correlation coefficient distribution indicated a sign-periodic fluctuation. These periodic regions of high correlation indicate that velocity fluctuations in those areas are independent of the velocity direction. For healthy flow conditions in HV2, the velocity fluctuations in the  $x$  and  $y$  directions are predominantly uncorrelated ( $<0.4$ ) in the region of the LHV wall jet. The lack of correlation is also present for velocity fluctuations along the streamline direction. This result is expected since the wall jet originates from the cross-flow collisions along the LHV–RHV plane. The uncorrelated regime observed in healthy flow condition disappeared at its pathological flow settings. As shown in Fig. 10, the fluctuations throughout the HV2



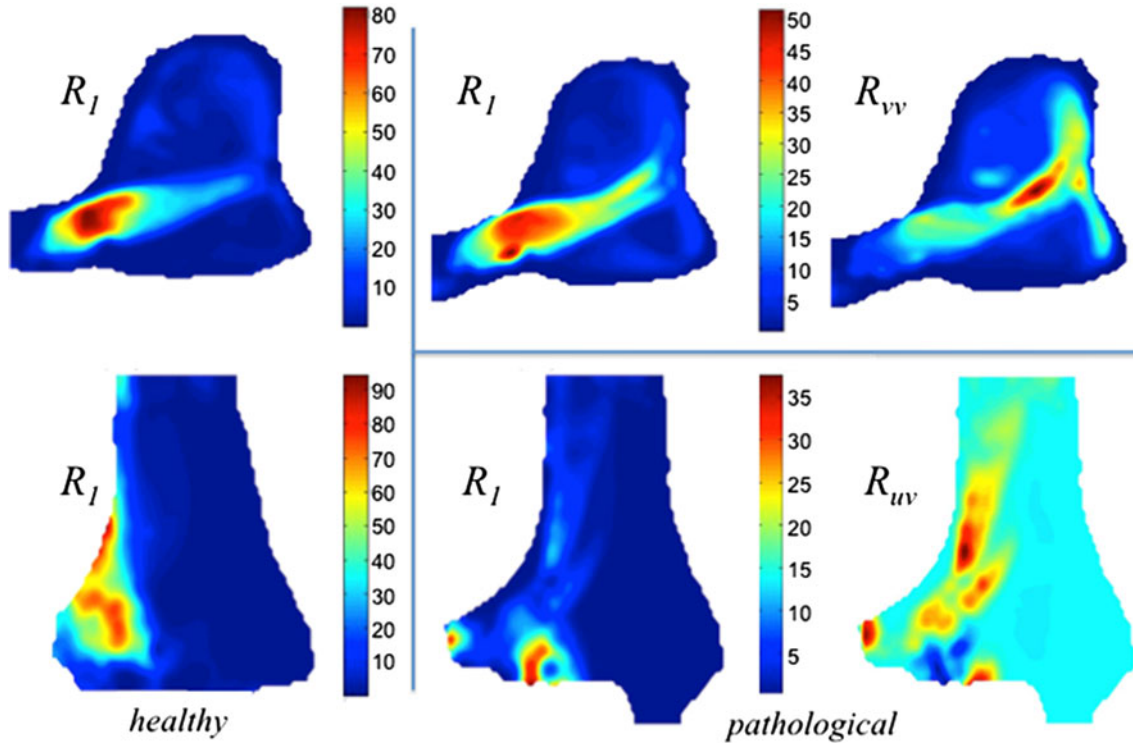


FIGURE 9. Unsteady flow regions are highlighted through the principal Reynolds shear stress ( $R_I$ ) distribution in hepatic vein models (HV1, top and HV2, bottom) for healthy (left) and pathological (right group) flow split conditions. For pathological flow selected Reynolds shear components ( $R_{uv}$  and  $R_{vv}$ ) are also presented. Single PIV slice is shown for each model. Units are in dyne/cm<sup>2</sup>.

geometry lose their “randomness” and become correlated for pathological flows. At the LHV inlet, there are large regions where streamwise correlation coefficients reach values as high as 0.7. The distribution of the streamwise correlation coefficient indicated that there exist regions in the vein models where the mean velocity fluctuations are strongly correlated in the direction of the streamlines of the average velocity field.

#### Effective Hepatic Junction Pressure Drop

The power loss and effective pressure drop for both junction geometries are significantly influenced by inlet flow conditions. As shown in Table 2, alteration of the flow splits from healthy to pathological settings results in a significant increase in the effective pressure drop across the vein junction. In HV1,  $\Delta P_{\text{EFF}}$  shifts from 10.22 to 18.11 mmHg, a 77% increase. In HV2,  $\Delta P_{\text{EFF}}$  increases from 6.37 to 7.22 mmHg, a 13% increase. The difference in magnitude of  $\Delta P_{\text{EFF}}$  between HV1 and HV2 is likely due to the orientation of the inlet vessels and the relative sizes of the two geometries. There was no significant change in  $\Delta P_{\text{EFF}}$  during these supplementary experiments where the total flow rate is

varied ( $\sim 0.7$ – $1.5$  L/min) at fixed flow split ratios, compared to the fixed flow rate experiments.

## DISCUSSION

In recent clinical literature, several interesting complex 3D cardiovascular flow regimes have been reported using primarily the phase-contrast (PC) MRI modality both for healthy and pathological flow conditions.<sup>5,20,21,36,47</sup> Unlike these phase-averaged flow regimes, the unsteady junction flow described in this study superimposed on the *mean* flow structure and therefore would be difficult to capture with standard PC-MRI sequences. Compared to the PC-MRI technique, *in vitro* PIV is therefore a more suitable tool to investigate such flow regimes. The patient-specific pediatric hepatic vein junction anatomies studied here represent two distinct structural configurations of the 3-inlet 1-outlet confluence of the main hepatic veins to the IVC. Even at moderate steady inflow conditions, PIV measurements demonstrate that complex unsteadiness can develop locally in anatomical multi-inlet venous confluences. For the hepatic junction, the distinct jet flow structures and accompanying shear layer interactions are the main driver of the observed

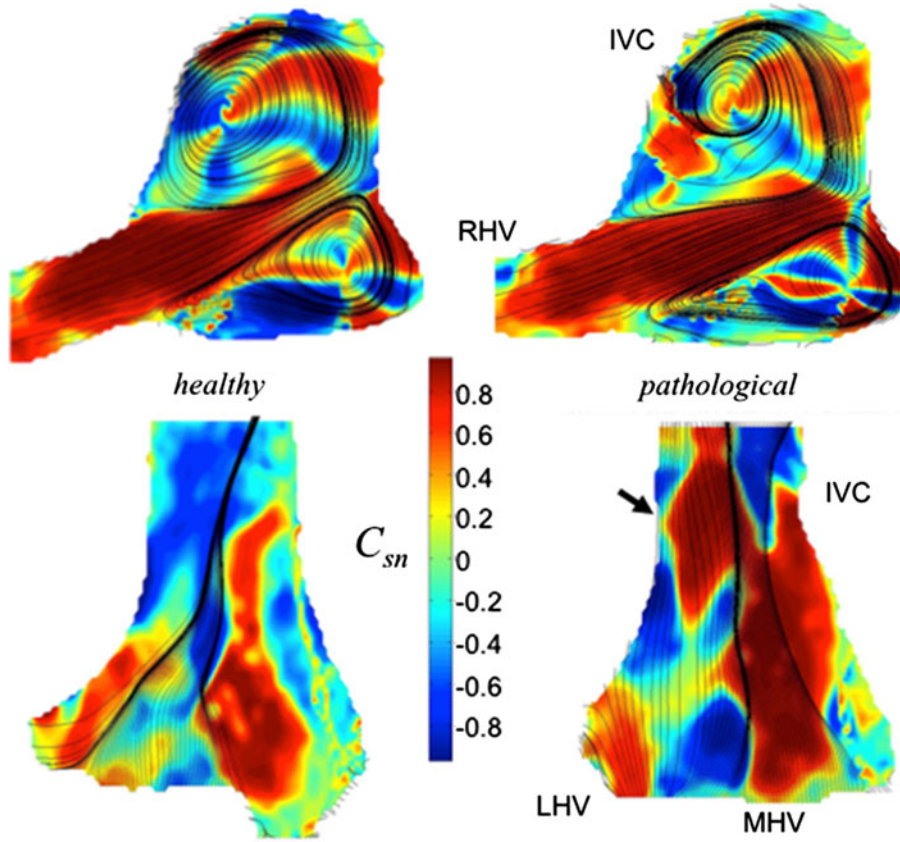


**FIGURE 10.** Contour plots of streamwise velocity correlation  $C_{sn}$  for HV1 (top row) and HV2 (bottom row) at healthy (left) and pathological (right) flows regimes. The velocity fluctuations are highly correlated for pathological flows. Both correlation coefficients remain high in the jet region. Corresponding average 2D streamlines are also displayed.

**TABLE 2.** Effective pressure drop for the venous junction anatomies (HV1 and HV2).

Flow rate (L/min)	Effective pressure drop ( $\Delta P_{EFF}$ )	
	HV1	HV2
1.0 (H)	6.37	10.22
1.0 (P)	7.22	18.11
0.76	6.94	16.70
0.95	6.52	16.45
1.14	6.92	16.99
1.51	6.79	16.16

Comparison between healthy (H) and pathological (P) flow settings indicates that  $\Delta P_{EFF}$  is significantly affected by the inlet flow splits for the range of flow rates studied.

instabilities. Physiological significance of these regimes requires further investigation, primarily if the junction flow condition influences the downstream IVC flow and pulmonary growth factor convection that is secreted from the liver. The fluid dynamics resulting from this confluence component can impart increased shear stress on the endothelium affecting the net hydraulic resistance and right ventricle preload.

Reynolds shear stress calculations revealed a consistent decrease in local unsteadiness and a global loss of fluid structure organization between healthy and pathological flows. In both HV1 and HV2, the maximum principal Reynolds shear stress value decreased when the inlet flow splits were changed from healthy settings to pathological settings. This decrease in fluid unsteadiness was more pronounced for HV2 geometry than for HV1 geometry, which is likely the result of the relative positions of the LHV and RHV inlets and the offset position of the MHV. The decrease in local fluid unsteadiness for HV1 can be attributed to the decrease in the relative differences between the inlet flows. The flow shift between healthy and pathological parameters reduces the maximum difference between the inlet flows to 10% of total IVC outflow compared to the 20% of IVC flow difference present in healthy flow. Unlike local unsteadiness, which decreases for both HV1 and HV2 between healthy and pathological flows, organization of the apparent fluid structures is markedly different between HV1 and HV2 geometries. HV2 velocity field for HV2 show that for pathological flow, the wall jet does not maintain its shape and wall localization as demonstrated for healthy flows. When

the inlet flow settings are changed from healthy to pathological, the jet becomes unstable, delocalizing from the left wall and extending into the center of the venous junction. Also, instead of coherently localized flow structures, the pathological jet-core exhibits multiple high velocity regions scattered throughout the wall jet region. This pattern is absent in HV1 geometry, where the RHV jet exhibits the same spatial characteristics for both healthy and pathological flows despite the variation of inlet flow distribution.

The apparent difference in flow organization can be attributed to the orientation of the inlet flows with respect to the mixing region of the confluence. For HV2, the LHV and RHV are oriented in a cross-flow arrangement. The MHV does not participate because it is oriented in an out-of-plane position and offset from the LHV–RHV mixing plane such that the surface normal of the MHV inlet is parallel to the wall jet axis. This configuration constrains the flow streams from the cross-flow resulting in a 90° turn towards the IVC. In HV1, all three inlet flows lie in the same plane as they drain into the hepatic pouch. Unlike HV2, the RHV inlet jet does not directly “collide” with any other jet. The velocity magnitude plots show that it intersects the middle jet, which originates from the MHV, and curves along the wall towards the IVC outlet. The difference in stability of these characteristic jets is best illustrated by the jet profiles, where the HV1 jet manifests the classical “plug-to-parabolic” evolution for both flow settings, whereas, HV2 exhibits a “twin-peak” shape for pathological settings. These results suggest that the in-plane configuration imposes greater hemodynamic stability than the cross-flow offset configuration.

The calculated values for integrated mean viscous shear stress and exposure time indicate that blood flow in both vein geometries experiences low magnitude shear stress for very short time periods. Since the integrated mean viscous shear stress remains on the order of 10 dyne/cm<sup>2</sup> for both HV1 and HV2 for all experiments, changing the flow conditions from healthy to pathological does not significantly alter the hemolysis potential due to viscous stress. The flows also do not likely correspond to significant blood damage conditions due to the very short exposure times.<sup>39,78</sup> Paul *et al.*<sup>53</sup> reported that for exposure times ranging between 25 and 1250 ms, for a minimum shear stress of 300 dyne/cm<sup>2</sup>, the maximum hemolysis, characterized by the hemolysis index (HI), reaches 3.5%. Since the median exposure time calculated from the present PIV measurements is only 3.5 ms, it is unlikely that blood damage is significant for either anatomical junction.

Submerged jets are characterized by four distinct states as a function of the  $Re$  number. To be succinct,

only the state with the lowest  $Re$  values ( $<300$ ) is relevant for this study. Jets within this range of  $Re$  are dissipated-laminar jets. They are unstable because the inlet jet momentum is quickly dissipated to the surrounding fluid resulting in loss of the initial jet shape and velocity.<sup>45</sup> McNaughton *et al.*<sup>45</sup> reports that jets of this type typically extend less than six diameters beyond the inlet before breaking down. Although jet penetration depth increases with larger  $Re$  numbers, it always undergoes Kelvin–Helmholtz instability before fully dissipating. Numerical simulations by Danaila *et al.*<sup>11</sup> for circular jets show that at a critical  $Re$  number of 225 different types of flow instabilities are exhibited. Beyond the critical  $Re$  number, the azimuthal velocity component ( $V_\theta$ ) oscillates with exponentially increasing amplitude over time due to the Kelvin–Helmholtz instability, characterized by periodically shedding vortex tubes. Silcock<sup>63</sup> determined an analytical solution for the stability of the Bickley jet, which is a plane jet flow configuration. Using linear stability theory this study showed that the even flow mode reaches a point of marginal stability at a  $Re$  of 10 for a wave-number of about 0.2. In practice this means that at  $Re = 10$ , if a sinusoidal disturbance is introduced to the flow at a wavelength of 10 m the jet flow would become unstable and transition to either a turbulent flow or a secondary instability state. The jets structures observed in our study are exposed to flow from two other confined inlet jets. In addition to the RHV jet, the presence of confining walls and opposing jet streams results in the development of multiple shear layers and flow disturbances in the junction geometry, thereby contributing to the observed unsteadiness. For the case of impinging circular jets similar to those observed in the hepatic venous junction, Gautner *et al.*<sup>22</sup> reported that wall influence becomes apparent only at about 2 jet diameters from the impinging surface. Consequently, an impinging jet is much like a free incompressible jet stream until the immediate vicinity of the impinging surface. This suggests that the temporal oscillations of the jet observed away from the impinging walls are indeed associated with the dissipative jet regime. Additionally, the experimental study of Ouwa *et al.*<sup>51</sup> reported that symmetric confined jets begin to show asymmetric flow patterns after a  $Re$  number of 30, supporting the fact that temporal oscillations are prevalent in the hepatic venous junction.

The results for effective pressure drop experiments indicate that total power loss and hydraulic resistance of both hepatic venous junctions depend significantly on subject-specific anatomy with high sensitivity to inlet flow conditions. Shifting inlet flow rates from healthy to pathological flow resulted in an increase in the effective pressure drop for both models. This effect was most apparent in the HV2 geometry, which



increased from 10.2 to 18.1 mmHg. The magnitude of the effective pressure drops was directly correlated with the loss of fluid structure that results from the inlet flow shift. The drastic increase in the effective pressure drop of HV2 is a result of the unstable flow characteristics that manifest for pathological flows. As discussed, the pathological flows for HV2 are characterized by delocalization of the LHV wall jet from the left wall towards the middle of the vein junction as well as increased mixing in the cross-flow region. Delocalization of the LHV jet and equalization of the two cross-flow jet flow rates creates large unstable regions throughout the flow field, resulting in lower pressure at the IVC outlet. The opposite is true for pressure drop across the HV1 geometry. The healthy flow structures for HV1 are not significantly altered when the inlet flow rates are shifted. The only measurable changes are a decrease in the maximum Reynolds stress of the RHV and middle jets. The stability of the flow field relative to the two flow settings explains the negligible increase in effective pressure drop.

The experiments measuring the sensitivity of effective pressure drop to total inlet flow suggest that the total pressure drop and power loss across the hepatic junction is significantly influenced by the inlet flow splits. Despite varying the total flow rate, the pressure drop did not change significantly for either junction model. This is an interesting finding because it implies that optimal performance of the pediatric hepatic venous outflow is primarily governed by the inflow flow conditions of the hepatic confluence drained from the major hepatic veins that pose both constant and pulsatile flow conditions.

This study has acknowledged limitations due to the experimental techniques implemented to replicate and visualize the flow fields in both pediatric hepatic junction anatomies. First, average steady flow conditions are emphasized to isolate the flow instabilities and fluctuations associated only with the model geometry. Pulsatile flow would likely to influence the reported unsteady flow structures. There is no consensus in the clinical literature regarding exact physiological pediatric hepatic waveforms; a high degree of variability is reported for physiological hepatic waveform phases. The second source of limitation is due to the employment of a two-component PIV system to study a 3D flow. The additional experimental complexity introduced by the stereoscopic PIV configuration is not justified in this study since the accuracy of out-of-plane component in standard three-component PIV technique is theoretically 4–9 times lower compared to the in-plane velocity components.<sup>40</sup> This limitation may be addressed through a tomographic 3D PIV set-up that employs at least 3 cameras (4 cameras in general). Therefore, in order to realize

high-quality velocity field measurements in two velocity components, the out-of-plane velocity component is forfeited. As a further remedy, in order to reduce the out-of-plane velocity components, the image planes were oriented along the major jet structures and multiple PIV planes are acquired. The third limitation is associated with the vessel compliance that possibly dampens and alters the *in vitro* rigid vessel measurements presented in this manuscript. Conversely, the reported velocity fluctuations have potential to induce vessel wall flutter. A fourth issue is related to the steadiness of the pump. We have tested the inflow flow steadiness with a time-resolved transonic inline probe and found that oscillations due to the pump are insignificant. At a typical inlet velocity, the standard deviation of velocity is less than 2%. In contrast the velocity fluctuations inside the model, i.e., the standard deviation in velocity range from 9 to 44% (arbitrary points selected in the PIV plane: 8.8, 10.6, 13.7, 14.6, 17.6, 16.1, 19.1, 21.4, and 43.8%). Spurious flow disturbances can also be generated in our flow loop from the anatomical-to-circular cross-section transitions due to diameter and shape mismatch. These small protrusions will become more critical for experiments operating at higher  $Re$  numbers ( $Re > 2000$ ). In our model the transition couplers are located far upstream and also very small in size (since in our case the pipe thickness is almost identical to the model thickness). Therefore, any residual mismatch will act as a small wall disturbance, which will eventually die-out in laminar pipe flow. The rapid-prototype model has ~10 extra diameters that would allow enough distance to stabilize these small disturbances. Finally, this study focused on the three major veins, which contribute a significant portion of the IVC outflow. The reconstructions selected for this study did not consider the presence of the minor hepatic veins, which have been known to exist in some subjects. Additional venous inlets would enhance the multifarious flow complexity, but complicate the flow loop design and feature similar unsteady flow structures.

Besides the basic hemodynamic understanding provided, the present experimental results can be utilized as challenging test case templates for ongoing efforts in cardiovascular computational fluid dynamics (CFD) solver development, particularly for test cases that require unsteady characteristic boundary conditions.

## CONCLUSIONS

This study characterizes the flow dynamics of multi-inlet patient-specific pediatric hepatic venous junctions. The significant findings were: (1) the in-plane/out-of plane configuration of the major hepatic veins contributes significantly to the mixing structure and



stability of the jet flows within the hepatic junctions even at steady inlet flow conditions; and (2) the flow dependency of total power loss for the venous junctions is primarily governed by the flow splits at the hepatic veins and is largely independent of total inlet flow rate. The sensitivity of the total confluence hemodynamics to inlet vessel orientation results from the unsteady internal fluid structures that are strongly dependent on both vessel anatomy and inlet flow conditions. (3) The low values for mean shear stress and exposure time indicate that the unstable mixing flow does not likely result in significant hemolysis at the confluence. The measured field characteristics provide a benchmark for clinical studies involving surgical optimization of visceral hemodynamics as well as experimental validation for numerical studies of anatomical confluences. Presently, the accuracy of computational simulations depends on the performance of inlet and outlet boundary conditions derived from lumped parameter models and the unsteady Bernoulli equation. The present experimental study can be further generalized to venous confluences with variable inlets and outlets, such as the hepatic/portal venous network. From a circulatory network system perspective, the 3D flow characteristics at the hepatic junction determine the organ flow split and enables a balanced compartmental organ perfusion. The “flow regime” of this confluence regulates the pressure levels at the upstream organ outlets and influences perfusion. As such, more uniform junction flow will lead to a totally different compartmental organ flow split compared to a disturbed flow condition at the junction. Likewise, 3D stagnation regions and jet-collisions will influence upstream organ perfusion and its regulation. Altered flow conditions can result abnormal vascular morphologies and unbalanced organ growth. Understanding of hepatic hemodynamics is relevant to the treatment of congenital heart defects, especially with regards to single-ventricle congenital heart disease. Extending this study to the optimization of surgically reconstructed venous junctions and including the entire sub-diaphragm vascular network magnifies the potential for improved hemodynamic performance and increased quality of life.

#### ACKNOWLEDGMENTS

The study was partially supported through NSF CAREER 0954465, Pennsylvania Infrastructure Technology Alliance (PITA) and SURG: Small Undergraduate Research Grants of Carnegie Mellon University. Anatomical patient-specific data used in this research study is provided through NIH HL67622.

#### REFERENCES

- <sup>1</sup>Abramovich, G. The Theory of Turbulent Jets. Cambridge: MIT Press, 1963.
- <sup>2</sup>Adrian, R. Dynamic ranges of velocity and spatial resolution of particle image velocimetry. *Meas. Sci. Technol.* 8:1393–1398, 1997.
- <sup>3</sup>Bale-Glickman, J., K. Selby, D. Saloner, and O. Savaş. Experimental flow studies in exact-replica phantoms of atherosclerotic carotid bifurcations under steady input conditions. *J. Biomech. Eng.* 125(1):38–48, 2003.
- <sup>4</sup>Barbe, T., J. Losay, G. Grimon, D. Devictor, A. Sardet, F. Gauthier, D. Houssin, and O. Bernard. Pulmonary arteriovenous shunting in children with liver disease. *J. Pediatr.* 126(4):571–579, 1995.
- <sup>5</sup>Bogren, H., and M. Buonocore. Complex flow patterns in the great vessels: a review. *Int. J. Card. Imaging* 15:105–113, 1999.
- <sup>6</sup>Bradshaw, P., D. Ferriss, and R. Johnson. Turbulence in the noise-producing region of a circular jet. *J. Fluid Mech.* 19:591–624, 1964.
- <sup>7</sup>Carnevale, F., A. Machado, M. Moreira, M. De Gregorio, L. Suzuki, U. Tannuri, N. Gibelli, J. Maksoud, and G. Cerri. Midterm and long-term results of percutaneous endovascular treatment of venous outflow obstruction after pediatric liver transplantation. *J. Vasc. Interv. Radiol.* 19:1439–1448, 2008.
- <sup>8</sup>Cheng, Y., T. Huang, C. Chen, T. Chen, C. Huang, S. Ko, and T. Lee. Variations of the left and middle hepatic veins: application in living related hepatic transplantation. *J. Clin. Ultrasound* 24:11–16, 1996.
- <sup>9</sup>Chiu, J. J., and S. Chien. Effects of disturbed flow on vascular endothelium: pathophysiological basis and clinical perspectives. *Physiol. Rev.* 91(1):327–387, 2011.
- <sup>10</sup>Chong, C., C. Rowe, S. Sivanesan, A. Rattray, R. Black, A. Shortland, and T. How. Computer aided design and fabrication of models for in vitro studies of vascular fluid dynamics. *Proc. Inst. Mech. Eng. H* 213:1–4, 1999.
- <sup>11</sup>Danalia, I., J. Dusek, and F. Anselmet. Coherent structures in a round, spatially evolving, unforced, homogeneous jet at low Reynolds numbers. *Phys. Fluids* 9(11):3323–3342, 1997.
- <sup>12</sup>Dasi, L., K. Whitehead, K. Pekkan, D. de Zelicourt, K. Sundareswaran, K. Kanter, M. Fogel, and A. Yoganathan. Pulmonary hepatic flow distribution in total cavopulmonary connections: extra-cardiac versus intra-cardiac. *J. Thorac. Cardiovasc. Surg.* 14:207–214, 2011.
- <sup>13</sup>de Zelicourt, D., K. Pekkan, H. Kitajima, D. Frakes, and A. Yoganathan. Single-step stereolithography of complex anatomical models for optical flow measurements. *J. Biomech. Eng.* 127:204–207, 2005.
- <sup>14</sup>Duncan, B., and S. Desai. Pulmonary arteriovenous malformations after cavopulmonary anastomosis. *Ann. Thorac. Surg.* 76:1759–1766, 2003.
- <sup>15</sup>Dur, O., E. Kocyildirim, O. Soran, P. Wearden, V. Morell, C. DeGroff, and K. Pekkan. Pulsatile venous waveform quality affects the conduit performance in functional and “failing” Fontan circulations. *Cardiol. Young* 2010 (in press).
- <sup>16</sup>Ensley, A., P. Lynch, G. Chatzimavroudis, C. Lucas, S. Sharma, and Y. Yoganathan. Toward designing the optimal total cavopulmonary connection: an in vitro study. *Ann. Thorac. Surg.* 68:1384–1390, 1999.
- <sup>17</sup>Ensley, A., A. Ramuzat, T. Healy, G. Chatzimavroudis, C. Lucas, S. Sharma, R. Pettigrew, and A. Yoganathan.

- Fluid mechanic assessment of the total cavopulmonary connection using magnetic resonance phase velocity mapping and digital particle image velocimetry. *Ann. Biomed. Eng.* 28:1172–1183, 2000.
- <sup>18</sup>Fallon, A., L. Dasi, U. Marzec, S. Hanson, and A. Yoganathan. Procoagulant properties of flow fields in stenotic and expansive orifices. *Ann. Biomed. Eng.* 36:1–13, 2008.
  - <sup>19</sup>Fallon, A., N. Shah, U. Marzec, J. Warnock, A. Yoganathan, and S. Hanson. Flow and thrombosis at orifices simulating mechanical heart valve leakage regions. *J. Biomech. Eng.* 128:30–39, 2006.
  - <sup>20</sup>Frydrychowicz, A., T. Bley, S. Dittrich, J. Hennig, M. Langer, and M. Markl. Visualization of vascular hemodynamics in a case of a large patent ductus arteriosus using flow sensitive 3D CMR at 3T. *J. Cardiovasc. Magn. Reson.* 9:585–587, 2007.
  - <sup>21</sup>Frydrychowicz, A., E. Weigang, M. Langer, and M. Markl. Flow-sensitive 3D magnetic resonance imaging reveals complex blood flow alterations in aortic Dacron graft repair. *Interact. CardioVasc. Thorac. Surg.* 5:340–342, 2006.
  - <sup>22</sup>Gauntner, J., N. B. Livingood, P. Hrycak. Survey of literature on flow characteristics of a single turbulent jet impinging on a flat plate. NASA TN D-5652 Lewis Research Center, USA, 1970.
  - <sup>23</sup>Ge, L., L. Dasi, F. Sotiropoulos, and A. Yoganathan. Characterization of hemodynamic forces induced by mechanical heart valves: Reynolds vs viscous stresses. *Ann. Biomed. Eng.* 36:276–297, 2007.
  - <sup>24</sup>George, S. Hemodynamic investigation of the liver using magnetic resonance imaging and computational fluid dynamics. Atlanta: Georgia Institute of Technology, 2008.
  - <sup>25</sup>Grigioni, M., A. Amodio, C. Daniele, G. D'Avenio, R. Formigari, and R. DiDonato. Particle image velocimetry analysis of the flow field in the total cavopulmonary connection. *Artif. Organs* 24:946–952, 2000.
  - <sup>26</sup>Hayashi, K., and T. Naiki. Adaptation and remodeling of vascular wall; biomechanical response to hypertension. *J. Mech. Behav. Biomed. Mater.* 2(1):3–19, 2009.
  - <sup>27</sup>Hjortdal, V., K. Emmertsen, E. Stenbog, T. Frund, M. Schmidt, O. Kromann, K. Sorensen, and E. Pedersen. Effects of exercise and respiration on blood flow in total cavopulmonary connection: a real-time magnetic resonance flow study. *Circulation* 108:1227–1231, 2003.
  - <sup>28</sup>Hsia, T., S. Khambadkone, J. Deanfield, J. Taylor, F. Migliavacca, and M. Leval. Surgery for congenital heart disease: subdiaphragmatic venous hemodynamics in the Fontan circulation. *J. Thorac. Cardiovasc. Surg.* 121:436–447, 2001.
  - <sup>29</sup>Hsia, T., S. Khambadkone, A. Redington, F. Migliavacca, J. Deanfield, and M. de Leval. Effects of respiration and gravity on infradiaphragmatic venous flow in normal and Fontan patients. *Circulation* 102(19 Suppl 3):148–153, 2000.
  - <sup>30</sup>Hughes, R., J. Watterson, C. Dickens, D. Ward, and A. Banaszek. Development of a nasal cast model to test medicinal nasal devices. *Proc. Inst. Mech. Eng. H* 222: 1013–1022, 2008.
  - <sup>31</sup>Hunter, K., C. Lanning, S. Chen, Y. Zhang, R. Garg, D. Ivy, and R. Shandas. Simulations of congenital septal defect closure and reactivity testing in patient-specific models of the pediatric pulmonary vasculature: a 3D numerical study with fluid-structure interaction. *J. Biomech. Eng.* 128:564–572, 2006.
  - <sup>32</sup>Jequier, S., J. Jequier, S. Hanquinet, J. Gong, C. Le Coultre, and D. Belli. Doppler waveform of hepatic veins in healthy children. *AJR Am. J. Roentgenol.* 175:85–90, 2000.
  - <sup>33</sup>Jequier, S., J. Jequier, S. Hanquinet, C. Le Coultre, and D. Belli. Hepatic vein Doppler studies: variability of flow pattern in normal children. *Pediatr. Radiol.* 32:49–55, 2002.
  - <sup>34</sup>Kaufmann, T., M. Hormes, M. Laumen, D. Timms, T. Schmitz-Rode, A. Moritz, O. Dzemali, and U. Steinseifer. Flow distribution during cardiopulmonary bypass in dependency on the outflow cannula positioning. *Artif. Organs* 33(11):988–992, 2009.
  - <sup>35</sup>Kiesewetter, C., N. Sheron, J. Vettukattill, N. Hacking, B. Stedman, H. Millward-Sadler, M. Haw, R. Cope, A. Salmon, M. Sivaprakasam, T. Kendall, B. Keeton, J. Iredale, and G. Veldtman. Hepatic changes in the failing Fontan circulation. *Heart* 93(5):579–584, 2007.
  - <sup>36</sup>Kilner, P., G. Yang, A. Wilkes, R. Mohiaddin, D. Firmin, and M. Yacoub. Asymmetric redirection of flow through the heart. *Nature* 404:759–761, 2000.
  - <sup>37</sup>Lambert, J. Hamolysierende Wirkung Hoher, Kurzzeitiger Schubspannungen. Aachen, Germany: RWTH Aachen, 1976.
  - <sup>38</sup>Lee, S., L. Antiga, and D. Steinman. Correlations among indicators of disturbed flow at the normal carotid bifurcation. *J. Biomech. Eng.* 131(6):061013, 2009.
  - <sup>39</sup>Leo, H., L. Dasi, J. Craberry, H. Simon, and A. Yoganathan. Fluid dynamic assessment of three polymeric heart valves using particle image velocimetry. *Ann. Biomed. Eng.* 34:936–995, 2006.
  - <sup>40</sup>Lindken, R., J. Westerweel, and B. Wieneke. Stereoscopic micro particle image velocimetry. *Exp. Fluids* 41:161–171, 2006.
  - <sup>41</sup>Liu, Q., D. Mirc, and B. M. Fu. Mechanical mechanisms of thrombosis in intact bent microvessels of rat mesentery. *J. Biomech.* 41(12):2726–2734, 2008.
  - <sup>42</sup>Long, J., A. Undar, K. Manning, and S. Deutsch. Viscoelasticity of pediatric blood and its implications for the testing of a pulsatile pediatric blood pump. *ASAIO J.* 51:563–566, 2005.
  - <sup>43</sup>Lonyai, A., A. Dubin, J. Feinstein, C. Taylor, and S. Shadden. New insights into pacemaker lead-induced venous occlusion: simulation-based investigation of alterations in venous biomechanics. *Cardiovasc. Eng.* 10(2):84–90, 2010.
  - <sup>44</sup>Loth, F., P. Fischer, N. Arslan, C. Bertram, S. Lee, T. Royston, W. Shaalan, and H. Bassiouny. Transitional flow at the venous anastomosis of an arteriovenous graft: potential activation of the ERK1/2 mechanotransduction pathway. *J. Biomech. Eng.* 125(1):49–61, 2003.
  - <sup>45</sup>McNaughton, K., and G. Sinclair. Submerged jets in short cylindrical flow vessels. *J. Fluid Mech.* 25:367–375, 1966.
  - <sup>46</sup>Mehran, R., R. Schneider, and P. Franchebois. The minor hepatic veins: anatomy and classification. *Clin. Anat.* 13:416–421, 2000.
  - <sup>47</sup>Morbiducci, U., R. Ponzini, G. Rizzo, M. Cadioli, A. Esposito, and A. Redaelli. In vivo quantification of helical blood flow in human aorta by time-resolved three-dimensional cine phase contrast magnetic resonance imaging. *Ann. Biomed. Eng.* 137(3):516–531, 2009.
  - <sup>48</sup>Murat, A., S. Akarsu, M. Cihangiroglu, H. Yildirim, S. Serhatlioglu, and O. Kalender. Assessment of Doppler waveform patterns and flow velocities of hepatic veins in children with acute viral hepatitis. *Diagn. Interv. Radiol.* 12:85–89, 2006.
  - <sup>49</sup>Nguyen, T., Y. Biadillah, R. Mongrain, J. Brunette, J. Tardif, and O. Bertrand. A method for matching the

- refractive index and kinematic viscosity of a blood analog for flow visualization in hydraulic cardiovascular models. *J. Biomech. Eng.* 126:529–535, 2004.
- <sup>50</sup>Oshinski, J. N., J. G. Delfino, P. Sharma, A. M. Gharib, and R. I. Pettigrew. Cardiovascular magnetic resonance at 3.0 T: current state of the art. *J. Cardiovasc. Magn. Reson.* 12:55, 2010.
- <sup>51</sup>Ouwa, Y., M. Watanabe, and Y. Matsuoka. Behavior of a plane jet at low Reynolds number confined in a rectangular channel. II. Two solutions by numerical analysis. *Jpn. J. Appl. Phys.* 25:1736–1740, 1986.
- <sup>52</sup>Patrick, M. J., C. Chen, D. H. Frakes, O. Dur, and K. Pekkan. Cellular-level near-wall unsteadiness of high-hematocrit erythrocyte flow using confocal  $\mu$ PIV. *Exp. Fluids* 50:887–904, 2011.
- <sup>53</sup>Paul, R., J. Apel, S. Klaus, F. Schugner, P. Schwindke, and H. Peul. Shear stress related blood damage in laminar couette flow. *Artif. Organs* 27:517–529, 2003.
- <sup>54</sup>Pekkan, K., L. Dasi, D. de Zélicourt, K. Sundareswaran, M. Fogel, K. Kanter, and A. Yoganathan. Hemodynamic performance of stage-2 univentricular reconstruction: Glenn vs. hemi-Fontan templates. *Ann. Biomed. Eng.* 37(1):50–63, 2009.
- <sup>55</sup>Pekkan, K., L. P. Dasi, P. Nourparvar, S. Yerneni, K. Tobita, M. A. Fogel, B. Keller, and A. Yoganathan. In vitro hemodynamic investigation of the embryonic aortic arch at late gestation. *J. Biomech.* 41(8):1697–1706, 2008.
- <sup>56</sup>Pekkan, K., D. de Zélicourt, L. Ge, F. Sotiropoulos, D. Frakes, M. A. Fogel, and A. P. Yoganathan. Physics-driven CFD modeling of complex anatomical cardiovascular flows—a TPCP case study. *Ann. Biomed. Eng.* 33(3):284–300, 2005.
- <sup>57</sup>Pekkan, K., O. Dur, K. Sundareswaran, K. Kanter, M. Fogel, A. Yoganathan, and A. Undar. Neonatal aortic arch hemodynamics and perfusion during cardiopulmonary bypass. *J. Biomech. Eng.* 130(6):061012, 2008.
- <sup>58</sup>Pekkan, K., H. Kitajima, D. de Zélicourt, J. Forbes, J. Parks, M. Fogel, S. Sharma, K. Kanter, D. Frakes, and A. Yoganathan. Total cavopulmonary connection flow with functional left pulmonary artery stenosis: angioplasty and fenestration in vitro. *Circulation* 112(21):3264–3271, 2005.
- <sup>59</sup>Ryu, K., T. Healy, A. Ensley, S. Sharma, C. Lucas, and A. Yoganathan. Importance of accurate geometry in the study of the total cavopulmonary connection: computational simulations and in vitro experiments. *Ann. Biomed. Eng.* 29:844–853, 2001.
- <sup>60</sup>Setyapranata, S., C. P. Brizard, I. E. Konstantinov, A. Iyengar, M. Cheung, and Y. d’Udekem. Should we always plan a Fontan completion after a Kawashima procedure? *Eur. J. Cardiothorac. Surg.* 2011 (in press) (1873–734X Electronic).
- <sup>61</sup>Sforza, D., C. Putman, and J. Cebral. Hemodynamics of cerebral aneurysms. *Annu. Rev. Fluid Mech.* 41:91–107, 2009.
- <sup>62</sup>Shah, M., J. Rychik, M. Fogel, J. Murphy, and M. Jacobs. Pulmonary AV malformations after superior cavopulmonary connection: resolution after inclusion of hepatic veins in pulmonary inclusion. *Ann. Thorac. Surg.* 63:960–963, 1997.
- <sup>63</sup>Silcock, G. On the Stability of Parallel Stratified Shear Flows. Ph.D. dissertation, University of Bristol, 1975.
- <sup>64</sup>Simon, H., L. Dasi, H. Leo, and A. Yoganathan. Spatio-temporal flow analysis in bileaflet heart valve hinge regions: potential analysis for blood element damage. *Ann. Biomed. Eng.* 35(8):1333–1346, 2007.
- <sup>65</sup>Someda, H., F. Moriyasu, M. Fujimoto, N. Hamato, M. Nabeshima, K. Nishikawa, M. Okuma, K. Tanaka, and K. Ozawa. Vascular complications in living related liver transplantation detected with intraoperative and postoperative Doppler US. *J. Hepatol.* 22:623–632, 1995.
- <sup>66</sup>Son, S. Y., K. D. Kihm, and J.-C. Han. PIV flow measurement for heat transfer characterization in two-pass square channels with smooth and 90 ribbled walls. *Int. J. Heat Mass Transfer* 45:4809–4822, 2002.
- <sup>67</sup>Sundareswaran, K., D. de Zélicourt, S. Sharma, K. Kanter, T. Spray, J. Rossignac, F. Sotiropoulos, M. Fogel, and A. Yoganathan. Correction of pulmonary arteriovenous malformation using image-based surgical planning. *JACC Cardiovasc. Imaging* 2:1024–1030, 2009.
- <sup>68</sup>Suwanprateeb, J., and W. Suwanpreuk. Development of translucent and strong three dimensional printing models. *Rapid Prototyping J.* 15(1):52–58, 2009.
- <sup>69</sup>Suzuki, L., I. Oliveira, A. Widman, N. Gibeli, F. Carnevale, J. Maksoud, A. Hubbard, and G. Cerri. Real-time and Doppler US after pediatric segmental liver transplantation. *Pediatr. Radiol.* 38:403–408, 2008.
- <sup>70</sup>Takata, M., and J. Robotham. Effects of inspiratory diaphragmatic descent on inferior vena caval venous return. *J. Appl. Physiol.* 72(2):597–607, 1992.
- <sup>71</sup>Tang, B., T. Fonte, F. Chan, P. Tsao, J. Feinstein, and C. Taylor. Three-dimensional hemodynamics in the human pulmonary arteries under resting and exercise conditions. *Ann. Biomed. Eng.* 39:347–358, 2010.
- <sup>72</sup>Teichgraber, U., M. Gebel, T. Benter, and M. Manns. Effect of respiration exercise, and food intake on hepatic vein circulation. *J. Ultrasound Med.* 16:549–554, 1997.
- <sup>73</sup>Tennekes, H., and J. Lumley. *A First Course in Turbulence*. Cambridge: MIT Press, 1972.
- <sup>74</sup>Van Steenkiste, C., B. Trachet, C. Casteleyn, D. van Loo, L. van Hoorebeke, P. Segers, A. Geerts, H. van Vlierberghe, and I. Colle. Vascular corrosion casting: analyzing wall shear stress in the portal vein and vascular abnormalities in portal hypertensive and cirrhotic rodents. *Lab. Invest.* 90(11):1558–1572, 2010.
- <sup>75</sup>Vignon-Clementel, I., A. Figueroa, K. Jansen, and C. Taylor. Outflow boundary conditions for 3D simulations of non-periodic blood flow and pressure fields in deformable arteries. *Comput. Methods Biomech. Biomed. Engin.* 13:625–640, 2010.
- <sup>76</sup>Walker, P., G. Oweis, and K. Watterson. Distribution of hepatic venous blood in the total cavo pulmonary connection: an in vitro study into the effects of connection geometry. *J. Biomech. Eng.* 123(6):558–564, 2001.
- <sup>77</sup>Wang, C., K. Pekkan, D. de Zélicourt, M. Horner, A. Parihar, A. Kulkarni, and A. Yoganathan. Progress in the CFD modeling of flow instabilities in anatomical total cavopulmonary connections. *Ann. Biomed. Eng.* 35(11):1840–1856, 2007.
- <sup>78</sup>Wurzinger, L., R. Opitz, and H. Eckstein. Mechanical blood trauma an overview. *Angeiologie* 38:81–97, 1986.
- <sup>79</sup>Yang, Y., S. George, D. Martin, A. Tannenbaum, and D. Giddens. 3D modeling of patient-specific geometries of portal veins using MR images. In: 28th IEEE EMBS Annual International Conference, 2006, pp. 5290–5293.